

Metamaterial-Based Octagonal Ring Penta-Band Antenna for Sub-6 GHz 5G, WLAN, and WiMAX Wireless Applications

Rishi Parasher, Dinesh Yadav*, and Ankur Saharia

Department of Electronics & Communication Engineering, Manipal University Jaipur, Jaipur, Rajasthan, India

ABSTRACT: In this article, a metamaterial SRR and CSRR based octagonal ring shaped multiband antenna is presented. The proposed antenna structure is designed with the implementation of slotted radiating patch with metamaterial cells for resonating at penta-bands to cover the 5G Sub-6 GHz NR frequency bands n48/n78/n79/n96, 3.5 GHz worldwide interoperability for microwave access, 5 GHz wireless local area network, 10.03–14.29 GHz upper X band, and 15.74–19.98 GHz upper Ku band wireless applications. The proposed antenna with a compact dimension of $33 \times 22 \times 1.6 \text{ mm}^3$ is fabricated to validate the simulated results with measured ones. The radiation characteristics is identified in stable and uniform manner for all the penta resonant bands.

1. INTRODUCTION

Presently, the boom in wireless communications require the 5G (fifth generation) technology mobile communication field with the features of high data rates, reduced latency, energy savings, lower costs and increased system capacity [1]. In 5G mobile communication, 5G Sub-6 GHz (5–6 GHz) band is defined to cover the various NR bands of wireless communication with advanced features as compared with the available 4G networks. The 5G frequency spectrum is identified into two formation of bands as lower than 6 GHz (FR1 NR bands) and more than 30 GHz regarding wireless standards [2]. The shift of antenna design from 4G to 5G band imposes the employment and investigation of various planer multiband antenna [3–5]. The development of frequency reconfigurable antenna for sub-6 GHz 5G and WLAN applications is ongoing, and the respective antenna design can be found in [3]. The work reported on 5G antenna design displayed the use of a magneto-electric dipole approach with broadband and high FBR (front to back ratio) characteristics in [4]. The multiple unit wideband MIMO antenna array approach is applicable to mobile devices to achieve the improvement in bandwidth and 5G NR communication bands [5, 37]. A slot-antenna array with wideband and high-isolation for multiple-input multiple-output (MIMO) systems is designed on an FR4 substrate to cover the fifth-generation new radio (5G NR) communication bands N77/N78/N79 [36]. A dual band low-profile quad-port printed antenna is proposed for 5G applications to utilize the 5G spectrum between 3.3 and 3.8 GHz, specifically in the n77 band, with a 10 dB bandwidth impedance [38]. By using various slotted, metamaterial loading, feeding techniques, multiband nature is created within single design [6–11]. The multiband feature is generated in antenna design with the implementation of metamaterial cells (SRR/CSRR) [12–15]. Another method of fractalization also provides the multiple wireless communi-

cation resonant band characteristics in antenna structure [16]. In [17–20], a hybrid fractal approach with metamaterial loading is introduced to achieve the multiple wireless standards.

To achieve penta band wireless and 5G NR bands, a metamaterial loaded slotted antenna design is proposed. The antenna has the optimized results for wireless applications worldwide interoperability for microwave access (3.5 GHz), Wireless local area network (5 GHz), higher range X/Ku band and 5G wireless communication standards. The antenna structure achieves five resonance characteristics at 3.19–3.96 GHz, 4.65–5.33 GHz, 6.78–7.54 GHz, 10.03–14.29 GHz, and 15.74–19.98 GHz to represent the wireless communication modes WiMAX (3.5 GHz), 5G FR1 NR Band (n48; 3.55–3.7 GHz and n78; 3.3–3.8 GHz), WLAN (5.0 GHz), 5G FR1 NR Band (n79; 4.67–5.0 GHz), 5G FR1 NR Band n96 (6.925–7.125 GHz), upper X band and upper Ku band respectively. The proposed design achieves resonance in a penta-band configuration, addressing various wireless standards, including 5G Sub-6 GHz NR Bands (5G FR1-n48/n78/n79/n96), WiMAX (3.5 GHz), WLAN (5.0), upper X band (10.03–14.29 GHz), and upper Ku band (15.74–19.98 GHz), as depicted in Figure 4. The frequency range of 3.19 to 3.96 GHz encompasses WiMAX (3.5 GHz) and 5G FR1 NR Band (n48; 3.55–3.7 GHz and n78; 3.3–3.8 GHz) wireless communication applications. The second resonating band, spanning 4.65–5.33 GHz, is designated for WLAN (5.0 GHz) and 5G FR1 NR Band (n79; 4.67–5.0 GHz) standards. The third and fourth resonating bands at 6.78–7.54 GHz and 10.03–14.29 GHz are linked to 5G FR1 NR Band n96 (6.925–7.125 GHz) and the upper X band, addressing terrestrial broadband and space communications applications. The fifth operating band of the proposed antenna design, ranging from 15.74 to 19.98 GHz, aligns with the upper Ku band for satellite communications applications.

* Corresponding author: Dinesh Yadav (dinesh.yadav@jaipur.manipal.edu).

TABLE 1. Parametric formation of ANN network.

Parameters	Values
Number of Neurons for First Input layer	2
Number of Neurons for second Intermediate layer	120
Number of Neurons for Third Output layer	4
Learning rate	0.0768
Number of epochs	1999
Training Algorithm	Levengberg-Marquardt (LM)

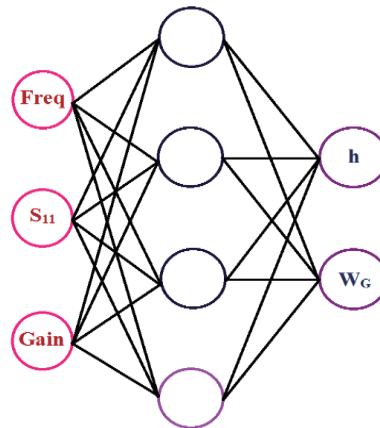


FIGURE 1. Machine learning network architecture.

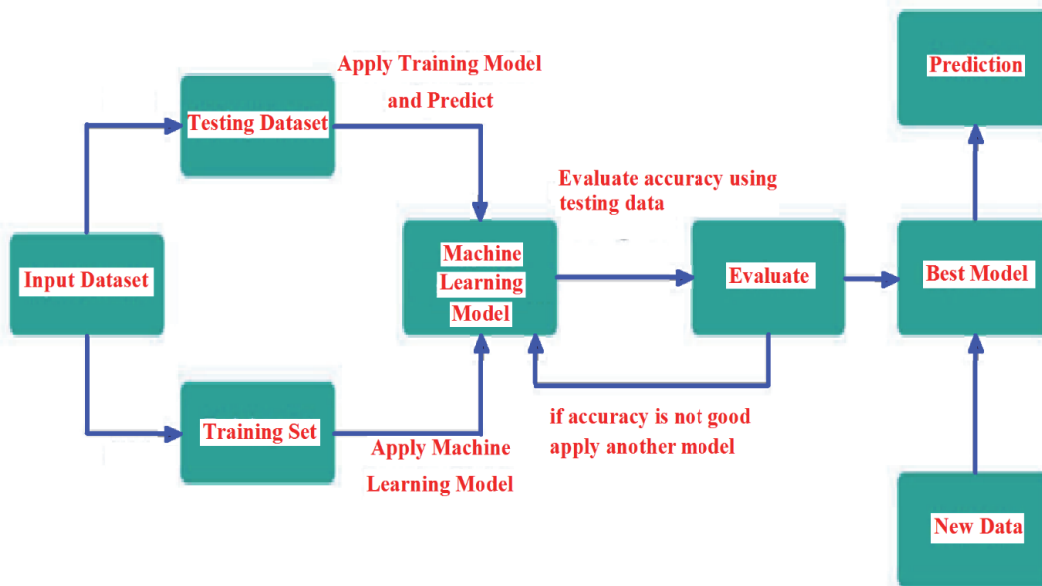


FIGURE 2. Flow Chart: Implementation of ML algorithms.

2. MACHINE LEARNING TECHNOLOGY

Over the past few decades, machine learning (ML) has made significant strides, finding frequent applications in work automation and bringing about a revolution in engineering and scientific techniques. In recent years, ML approaches have been extensively explored and adopted in antenna design, due

to their ability to learn from measured or simulated antenna data through a training procedure, thereby expediting the entire antenna design process [39]. When dealing with the tuning of multiple parameters or the design of complex structures, ML approaches offer substantial advantages by significantly reducing computing times [40].

TABLE 2. Proposed antenna's evolutionary development phases.

Antenna formations	Configuration of the Upper and Lower Segments in the Proposed Design	Resonating band (in GHz) during simulation and measurement mode	Bandwidth (in %) during simulation and measurement mode	Peak Gain (in dBi) during simulation and measurement mode	Efficiency (in %) during simulation and measurement mode	Modes of Wireless Applications Covered	Causes
A	Radiating Section: An octagonal slotted geometry connected to a trapezoidal -shaped feedline Ground part: Trapezoidal shape with Defected Ground Structure (DGS)	Sim.: 2.93–14.28 Meas.: 3.03–12.92	Sim.: 131.90 Meas.: 124.01	Sim.: 2.62 Meas.: 2.34	Sim.: 73.61 Meas.: 71.62	No. of Applications — 1 Single band (UWB)	The wideband characteristics are achieved through an octagonal slotted radiating patch and a trapezoidal-shaped Defected Ground Structure (DGS) ground component
B	Radiating Section: An octagonal slotted geometry connected to a trapezoidal -shaped feedline Ground part: Trapezoidal shape with Defected Ground Structure (DGS) loaded with rectangular SRR cell	Sim.: 2.99–7.63, 10.09–14.18, 16.52–19.98 Meas.: 3.05–7.22, 9.89–13.87, 17.52–19.47	Sim.: 87.38, 33.70, 18.96 Meas.: 81.20, 33.50, 10.54	Sim.: 2.78, 3.28, 3.46 Meas.: 2.01, 3.11, 2.37	Sim.: 79.68, 79.52, 82.36 Meas.: 75.84, 76.32, 81.21	No. of Applications — 3 Triple band (WLAN/WiMAX, upper X band, and upper Ku band)	The current perturbation effect arises from the slotted patch area and the presence of Split Ring Resonator (SRR) loaded defected ground plane.

C	Radiating Section: An octagonal slotted geometry connected with CSRR inspired trapezoidal shape feedline Ground part: Trapezoidal shape with Defected Ground Structure (DGS) loaded with rectangular SRR cell	Sim.: 3.19–3.96, 4.65–5.33, 6.78–7.54, 10.03–14.29, 15.74–19.98 Meas.: 3.28–3.97, 4.82–5.48, 6.84–7.59, 10.01–14.34, 15.68–19.74	Sim.: 21.54, 13.63, 10.61, 35.03, 23.74 Meas.: 19.03, 12.81, 10.39, 35.56, 22.92	Sim.: 2.51, 1.52, 1.51, 2.48, 3.58, 3.62 Meas.: 2.49, 0.86, 1.34, 2.23, 3.21, 3.32	Sim.: 81.28, 79.98, 82.34, 76.84, 86.52 Meas.: 74.92, 59.96, 75.68, 73.52, 81.79, 82.06	No. of Applications — 5 Penta a band (5G Sub-6 GHz NR Bands (5G FR1-n48/n78/n79/n96), WiMAX (3.5 GHz), WLAN (5.0), upper X band (10.03–14.29 GHz) and upper Ku band (15.74–19.98 GHz)	The slotted fractal-based patch structure is connected to a trapezoidal-shaped feedline inspired by CSRR and a trapezoidal-shaped ground plane with a loaded rectangular SRR cell. These elements contribute to the generation of current perturbations and negative permeability characteristics, aiming to achieve a penta-band resonating state for 5G wireless applications
---	--	---	---	--	---	--	---

After acquiring a dataset, it can be partitioned into two segments: training and cross-validation. The allocation of records to each segment is contingent on the total number of records in the dataset. In the suggested antenna model, 80 percent of the records are dedicated to the training set, while the remaining 20 percent are assigned to the cross-validation sets.

This article employs Artificial Neural Network (ANN) algorithms [41, 42] for making predictions. The selection of this algorithm is based on its ability to perform regression on non-linear data. As the desired output takes the form of numerical values, regression stands out as the most suitable method for prediction. The implementation of these algorithms is carried out in Python3 due to its ease of use and the availability of numerous libraries supporting data pre-processing, machine learning algorithms, and visualization.

Machine Learning (ML) technique is apply to extract the desired information from input information or data by using various types of algorithm approaches. These algorithms are based upon optimization method where the required optimized data can be identified from the input collected data. This technique is a collaboration of statistics and data analysis. In this work, the antenna design modelling and performance analysis are per-

formed by using back-propagation algorithms based machine learning network. This algorithm is executed into three formations as Formation I: During this, a number of simulations are performed with respect to various geometrical parameters of antenna with the help of simulation software [21] to attain the electromagnetic characteristics of proposed structure. Formation II: After formation I, the electromagnetic characteristics are converted into a database and applied to training process by using machine learning network. Formation III: when formations I and II are completed, such a network provides the optimized results of antenna design.

The artificial neural network (ANN) is designed by using three layers for incoming data, intermediate and outgoing data respectively as indicated in Figure 1. Here, the first layer is dedicated to various parameters; the second one is implemented upon incoming data with the help of 120 neurons; and the third layer is responsible for optimized data of antenna geometrical parameters (h and W_G). Initially, the dataset is generated by using CST simulator and applied for training, validation, and testing process with the help of an ANN network. The ANN network parametric observation is indicated in Table 1, and architecture is shown in Figure 1.

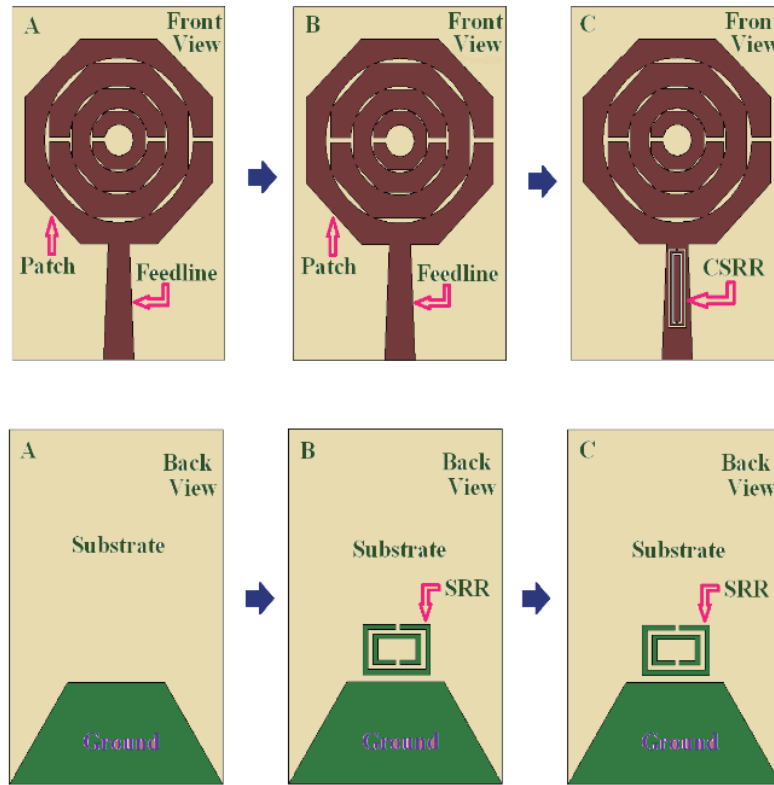


FIGURE 3. Design process of multiband antenna.

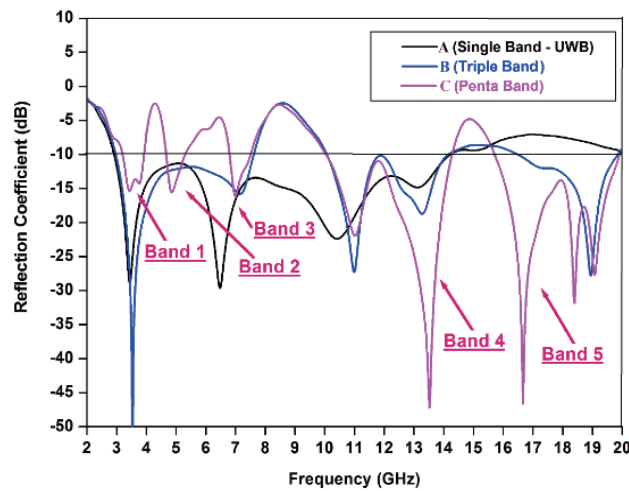


FIGURE 4. Simulated S_{11} results of configuration A, B and C.

To generate a dataset, the envisaged antenna is crafted using the CST EM simulator. This dataset becomes instrumental for making predictions. The simulation of the antenna focuses on two key parameters: the resonant frequency (Freq) and the return loss or reflection coefficient (S_{11}). Additionally, the gain of the antenna is also considered as a third parameter in the simulation.

Following simulations on CST, the results are gathered and stored. The dataset, obtained through antenna simulation, comprises 201 records with 1009 features. This dataset is generated by varying the antenna's geometrical parameters, specifically the height (h) and width (W_G). Subsequently, a new dataset is formulated, encompassing 202,608 records and featuring three key attributes: resonant frequency (Freq), return loss (dB), and gain at the resonant frequency.

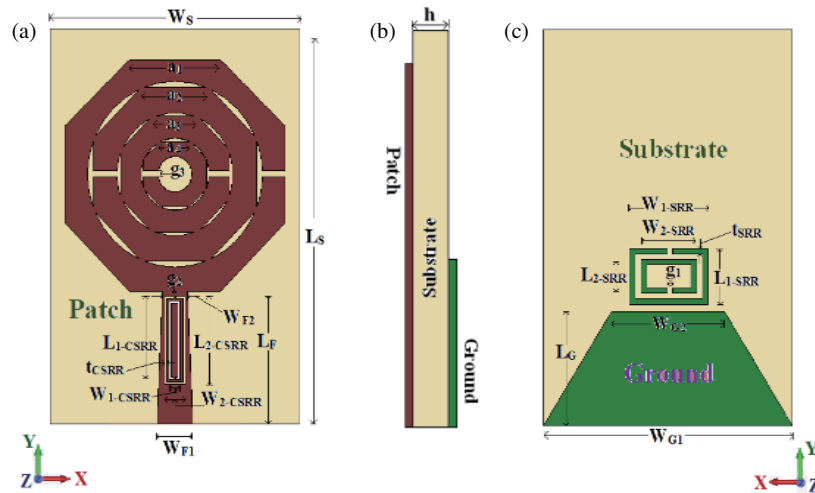


FIGURE 5. Geometrical formation of proposed design.

Dimensions	In mm
Substrate Length (L_S)	33
Substrate Width (W_S)	22
Height (h)	1.6
Feedline Length (L_F)	11
Feedline Width (W_{F1})	3.16
Feedline Width (W_{F2})	2
Slotted Length (a_3)	4
Slotted Length (a_4)	2.5
CSRR Length (L_{1-CSRR})	7.2
CSRR Width (W_{1-CSRR})	1
CSRR Length (L_{2-CSRR})	8
CSRR Width (W_{2-CSRR})	1.8
Ground Width (W_{G1})	22
Ground Width (W_{G2})	10
SRR Length (L_{1-SRR})	5.09
SRR Width (W_{1-SRR})	7.02
SRR Length (L_{2-SRR})	3.49
SRR Width (W_{2-SRR})	5.42
Slotted Length (a_1)	8
Slotted Length (a_2)	6
CSRR Gap (g_2)	0.2
Ground Length (L_G)	9.5
SRR Gap (g_1)	0.28
Slotted Gap (g_3)	0.5

TABLE 3. Optimized parameters.

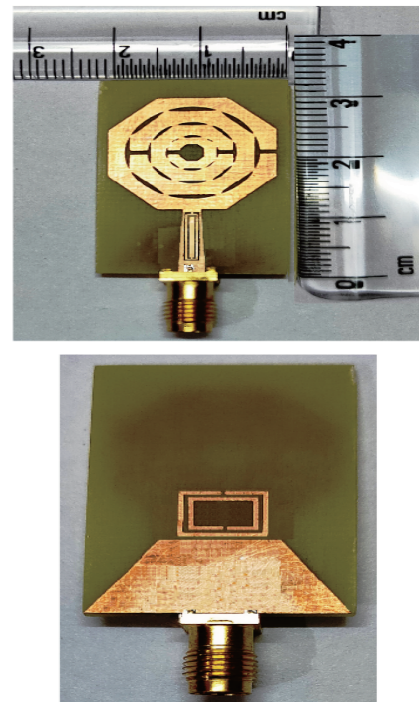


FIGURE 6. Fabricated formation of proposed antenna.

Figure 2 illustrates a flowchart detailing the implementation of the machine learning algorithm. Upon reviewing the dataset, we partitioned it into two segments: the first part constitutes the training set, while the second part forms the cross-validation set, following the guidelines in [43]. Subsequently, the training set is employed to train a machine learning algorithm, incorporating various features and labels. Once the model is trained and cross-validated, it becomes capable of predicting the loss at the resonating frequency for specified inputs. Through ma-

chine learning, predictions are accomplished with significantly reduced time and a lower error margin than CST simulation results.

Following the training of machine learning models using the CST dataset, the optimal model is chosen based on the highest R-square score and the lowest mean square error (MSE) value. Subsequently, the dataset is applied to this selected model to predict the S_{11} value. The parameters yielding the lowest S_{11} value are then identified.

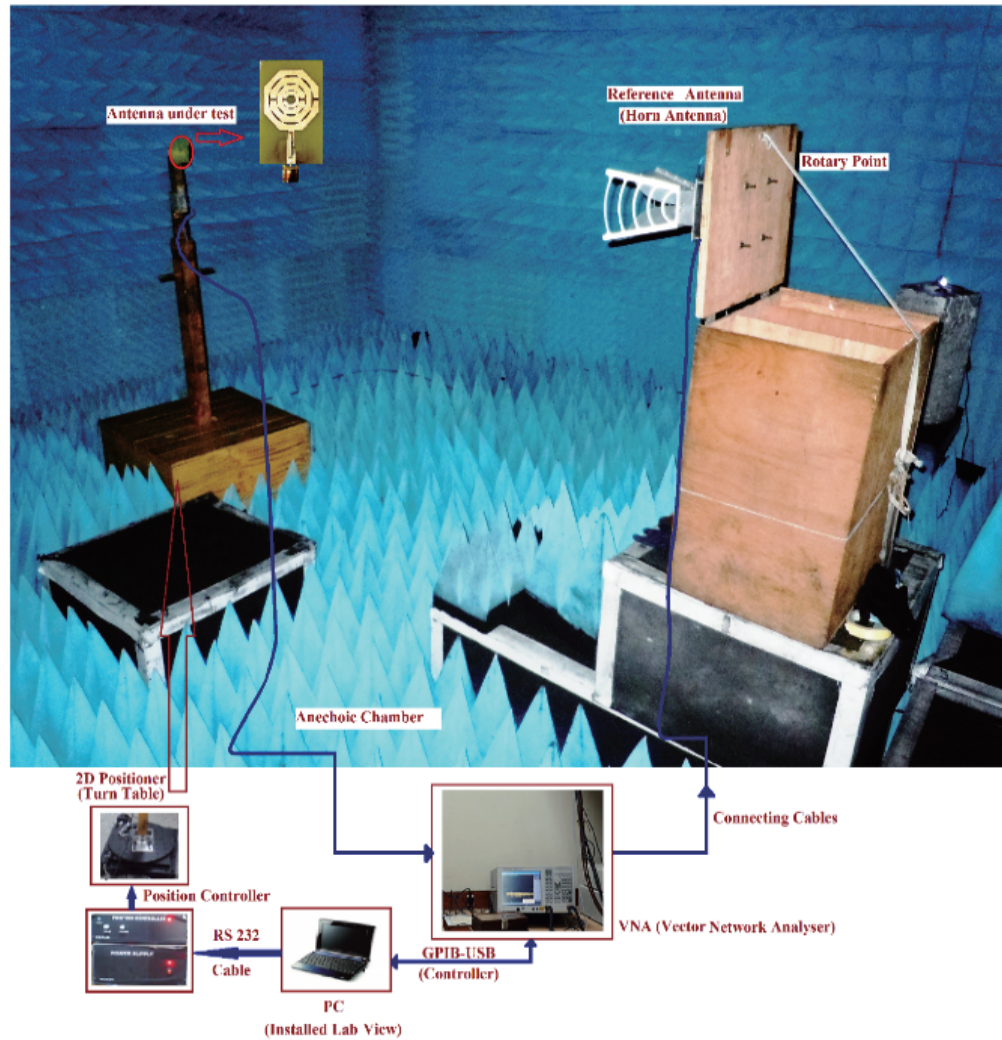


FIGURE 7. Measurement setup.

3. ANTENNA GEOMETRICAL OBSERVATION

The geometry of proposed antenna consisting of the trapezoidal shape ground and feedline with a slotted octagonal shape radiating patch. The patch and ground section are fabricated on a 1.6 mm thick dielectric substrate material of FR4 ($\epsilon_r = 44$ and $\tan \delta = 0.2$). The design process of the proposed antenna is identified on the basis of simulated S -parameter results from basic UWB antenna (A) to proposed multiband antenna (C) as shown in Figure 3. Table 2 presents the various characteristics of the antenna design from configurations A to C.

The proposed design achieves resonance in a penta-band configuration, catering to the following wireless standards: 5G Sub-6 GHz NR Bands (5G FR1-n48/n78/n79/n96), WiMAX (3.5 GHz), WLAN (5.0), upper X band (10.03–14.29 GHz), and upper Ku band (15.74–19.98 GHz), as illustrated in Figure 4. The operational band from 3.19 to 3.96 GHz covers WiMAX (3.5 GHz) and 5G FR1 NR Band (n48; 3.55–3.7 GHz and n78; 3.3–3.8 GHz) wireless communication applications. The second resonating band, spanning 4.65–5.33 GHz, is allocated to

WLAN (5.0 GHz) and 5G FR1 NR Band (n79; 4.67–5.0 GHz) wireless standards. The third and fourth resonating bands at 6.78–7.54 GHz and 10.03–14.29 GHz are associated with 5G FR1 NR Band n96 (6.925–7.125 GHz) and upper X band, covering terrestrial broadband and space communications applications. The fifth operating band of the proposed antenna design, ranging from 15.74 to 19.98 GHz, is relevant to the upper K_U band for satellite communications applications.

The geometrical formation of proposed multiband metamaterial antenna is indicated in Figure 5 with top, side, and bottom views. The optimized parameters of antenna are mentioned in tabular form in Table 3. Simulation results of antenna are achieved with the help of simulator CST Microwave Studio (CST MWS) software [21], and the antenna is fabricated accordingly, illustrated in Figure 6.

The measurement process can be performed in an anechoic chamber with VNA, as represented in Figure 7. From Figure 8, it is observed that there is good impedance matching over five operating bands during simulation and experimental pro-

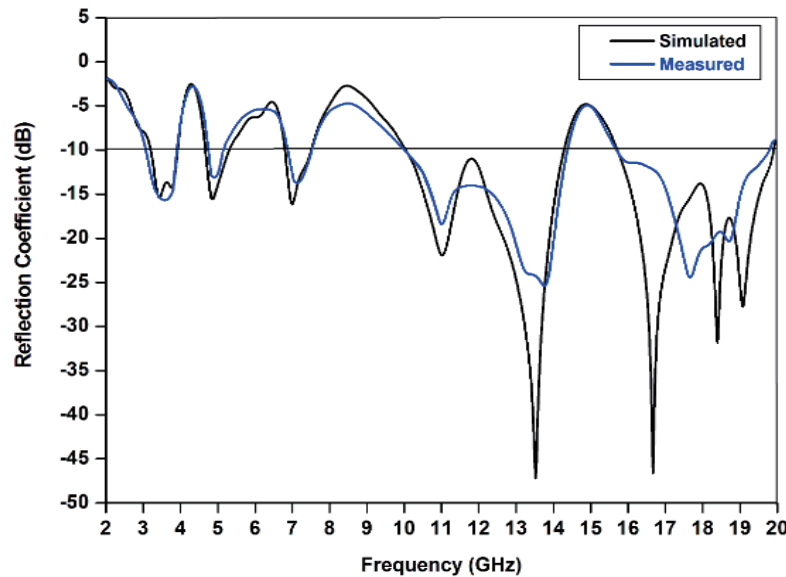


FIGURE 8. S parameters analysis during simulation and measurement mode.

cess. The simulated and measured antenna characteristics are observed in Table 4. It is noticed that there is good agreement between the simulated and measured results.

3.1. Physical Parametric Observations

To achieve the optimized dimensions of the proposed antenna, parametric study is performed regarding patch, ground, and feedline dimensions. The parametric study is focused on patch, feedline, SRR, and CSRR physical parameters. The relative comparison of the reflection coefficient for various physical dimensions of antenna is represented in Figures 9 to 13. It is noticed that the reflection coefficients vary according to the changes in physical parameters of the proposed design. The optimized dimensions with improved impedance matching are tabulated in Table 5.

The optimal design constraints and dimensions of the proposed SRR/CSRR design are determined through parametric analysis concerning SRR/CSRR dimensions, including length (L_{1-SRR} and L_{2-CSRR}) and width (W_{1-SRR} and W_{2-CSRR}). The comparison graph of the S_{11} parameter is examined for various values of CSRR dimensions, namely L_{2-CSRR} (7.6, 7.8, 8.0, 8.2 mm) and W_{2-CSRR} (1.6, 1.7, 1.8, 1.9 mm), as depicted in Figure 11. The graph clearly indicates that the optimal CSRR dimensions (length and width) yielding a significant antenna response are $L_{2-CSRR} = 8.0$ mm and $W_{2-CSRR} = 1.8$ mm, represented by the red and black lines in Figure 11, respectively.

By optimizing appropriate CSRR dimensions, the structure can achieve better impedance matching, leading to a noteworthy output at the claimed frequency. Another observation is that impedance matching improves when CSRR length L_{2-CSRR} increases, and width W_{2-CSRR} decreases in the lower frequency range (L_{2-CSRR} : below 12 GHz, W_{2-CSRR} : below

12 GHz). For the higher operating range (L_{2-CSRR} : above 12 GHz, W_{2-CSRR} : above 12 GHz), impedance matching is enhanced by decreasing CSRR length L_{2-CSRR} and increasing width W_{2-CSRR} .

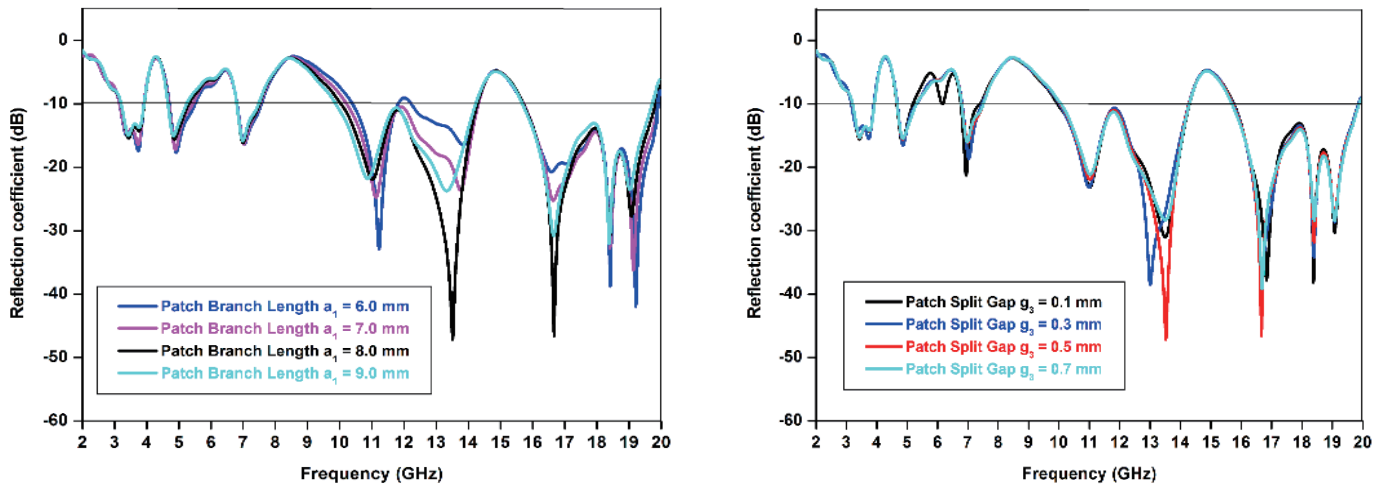
The S_{11} parameter comparison graph explores various dimensions of SRR, specifically L_{1-SRR} (4, 5, 5.09, and 6 mm) and W_{1-SRR} (6, 7, 7.02, and 8 mm), as illustrated in Figure 13. The graph clearly reveals that the optimal CSRR dimensions (length and width) for a significant antenna response are $L_{1-SRR} = 5.09$ mm and $W_{1-SRR} = 7.02$ mm, represented by the red and black lines in Figure 13, respectively. Through the optimization of these SRR dimensions, the structure attains improved impedance matching, resulting in a noteworthy output at the specified frequency. Additionally, it is observed that impedance matching is enhanced by decreasing SRR dimensions (L_{1-SRR} and W_{1-SRR}) in the lower frequency range (L_{1-SRR} : below 10 GHz, W_{1-SRR} : below 14 GHz). Conversely, in the higher operating range (L_{1-SRR} : above 10 GHz, W_{1-SRR} : above 14 GHz), impedance matching is improved by increasing SRR dimensions (L_{1-SRR} and W_{1-SRR}).

3.2. Study of SRR Structure

The simulated waveguide arrangement is implemented to study the SRR cell as illustrated in Figure 14. The proposed cell consists of two rectangle-shaped metallic rings with split gap. It is designed on an FR-4 substrate ($\epsilon_r = 4.4$, $\tan \delta = 0.02$) with dimensions $5.09 \times 7.02 \times 1.6$ mm³. A simulated waveguide arrangement is designed to retrieve the effective material parameters (permeability μ_{eff} /permittivity ϵ_{eff}), refractive index (n), and wave impedance (z). This setup is established in simulated environment with the help of simulator CST Microwave Studio (MWS) [21]. The SRR cell is placed between the two

TABLE 4. Performance analysis.

Resonating Modes	Frequency Band (in GHz)		Bandwidth (in %)		S parameter (S_{11}) (in dB)	
	Simulated	Experimental	Simulated	Experimental	Simulated	Experimental
1	3.19–3.96	3.28–3.97	21.54	19.03	–16.12	–16.14
2	4.65–5.33	4.82–5.48	13.63	12.81	–17.28	–13.41
3	6.78–7.54	6.84–7.59	10.61	10.39	–18.32	–14.21
4	10.03–14.29	10.01–14.34	35.03	35.56	–47.68	–25.72
5	15.74–19.98	15.68–19.74	23.74	22.92	–46.52	–24.92


FIGURE 9. Parametric study for patch parameters (branch length a_1 and gap g_3).

ports 1 and 2 boundary conditions as mentioned in Figure 14. Incoming EM waves are generated at port 1, pass through the SRR, and are received at port 2. By using this arrangement, the simulated S parameters retrieve S_{11} and S_{12} to calculate the effective dielectric parameter of the proposed SRR cell. An equivalent circuit of SRR cell is designed by using inductor L and capacitor C , which are connected into parallel formation. The metallic section of SRR is responsible for inductive L components whereas the split gap/slots between the metallic rectangular rings generates the capacitive C effect. Inside the setup, to obtain the measured S parameters (S_{11} and S_{12}), the proposed SRR is placed at the center location by using adaptors and connected with VNA [22].

Initially, port 1 is excited by EM waves, and these waves are passing to port 2 through SRR cell. Due to these waves, the conduction current is generated and flows from outer conducting ring to inner ring via gap. The metallic portion and gaps create the inductive and capacitive effect (distributed capacitance), respectively. The inductance and capacitance values provide the resonant frequency as follows [23];

$$f_{R-SRR} = \frac{1}{2\pi\sqrt{L_{TI}C_{TI}}} \quad (1)$$

where

$$L_{TI} = 0.0002 \left\{ 2(L_{Extrnal-SRR} + W_{Extenal-SRR}) - g_1 \right\} \left\{ (\log_e 8) \frac{(L_{Extrnal-SRR} + W_{Extenal-SRR} - 0.5g_1)}{t_{SRR}} \right\} - K \quad (2)$$

$$C_{TI} = 0.5 \left\{ (L_{Extrnal-SRR} + W_{Extenal-SRR}) - \pi(t_{SRR} + 0.5g') - g_1 \right\} \left\{ (0.3 \times 10^{-8})(\sqrt{\epsilon_e}/Z_0) \right\} + \left\{ (8.85 \times 10^{-12})h't_{SRR}/g_1 \right\} \quad (3)$$

where $L_{Extrnal-SRR}$ = Length (External rectangular SRR ring), $W_{Extrnal-SRR}$ = Width (External rectangular SRR ring), g_1 = Split gap, t_{SRR} = Thickness, K = Constant (2.4512), g' = Rectangular SRR ring's gap, ϵ_e = Effective permittivity of the medium, Z_0 = Characteristic impedance, h' = Height of the conducting strip.

The effective dielectric parameter (permeability: μ_{eff}) is identified from following equations [23, 24];

$$\mu_{eff} = n_r \times z_i \quad (4)$$

where

TABLE 5. Parametric observation for optimized dimensions of proposed structure.

Sr. No.	Physical dimensions		Impedance matching	Optimized value	
1	Radiating section Patch	Arm side length ($a_1 = 6$ mm, 7 mm, 8 mm, 9 mm)	Resonance spam (2 GHz to 12 GHz)	Enhanced: a_1 is decreases	8 mm
			Resonance spam (12 GHz to 20 GHz)	Enhanced: a_1 is increases	
		Split gap ($g_3 = 0.1$ mm, 0.3 mm, 0.5 mm, 0.7 mm)	Resonance spam (2 GHz to 12 GHz)	Enhanced: g_3 is decreases	0.5 mm
			Resonance spam (12 GHz to 20 GHz)	Enhanced: g_3 is increases	
2	Feedline parameters	Length ($L_F = 9$ mm, 10 mm, 11 mm, 12 mm)	Resonance spam (2 GHz to 12 GHz)	Enhanced: L_F is increases	11 mm
			Resonance spam (12 GHz to 20 GHz)	Enhanced: L_F is decreases	
		Width ($W_{F1} = 2.5$ mm, 3.0 mm, 3.16 mm, 3.5 mm, 4.0 mm)	Resonance spam (2 GHz to 12 GHz)	Enhanced: W_{F1} is increases	3.16 mm
			Resonance spam (12 GHz to 20 GHz)	Enhanced: W_{F1} is decreases	
		Width ($W_{F2} = 1.8$ mm, 2.0 mm, 2.2 mm, 2.4 mm)	Resonance spam (2 GHz to 12 GHz)	Enhanced: W_{F2} is increases	2.0 mm
			Resonance spam (12 GHz to 20 GHz)	Enhanced: W_{F2} is decreases	
3	CSRR parameters	Length ($L_{2-CSRR} = 7.6$ mm, 7.8 mm, 8.0 mm, 8.2 mm)	Resonance spam (2 GHz to 12 GHz)	Enhanced: L_{2-CSRR} is increases	8.0 mm
			Resonance spam (12 GHz to 20 GHz)	Enhanced: L_{2-CSRR} is decreases	
		Width ($W_{2-CSRR} = 1.6$ mm, 1.7 mm, 1.8 mm, 1.9 mm)	Resonance spam (2 GHz to 12 GHz)	Enhanced: W_{2-CSRR} is decreases	1.8 mm
			Resonance spam (12 GHz to 20 GHz)	Enhanced: W_{2-CSRR} is increases	
4	Ground Parameters	Length ($L_G = 8.5$ mm, 9.0 mm, 9.5 mm, 10.0 mm)	Resonance spam (2 GHz to 12 GHz)	Enhanced: L_G is increases	9.5 mm
			Resonance spam (12 GHz to 20 GHz)	Enhanced: L_G is decreases	
		Width ($W_{G1} = 20$ mm, 21 mm, 22 mm, 23 mm)	Resonance spam (2 GHz to 12 GHz)	Enhanced: W_{G1} is increases	22 mm
			Resonance spam (12 GHz to 20 GHz)	Enhanced: W_{G1} is decreases	
5	SRR dimensions	Length ($L_{1-SRR} = 4$ mm, 5 mm, 5.09 mm, 6 mm)	Resonance spam (2 GHz to 12 GHz)	Enhanced: L_{1-SRR} is decreases	5.09 mm
			Resonance spam (12 GHz to 20 GHz)	Enhanced: L_{1-SRR} is increases	
		Width ($W_{1-SRR} = 6$ mm, 7 mm, 7.02 mm, 8 mm)	Resonance spam (2 GHz to 12 GHz)	Enhanced: W_{1-SRR} is decreases	7.02 mm
			Resonance spam (12 GHz to 20 GHz)	Enhanced: W_{1-SRR} is increases	

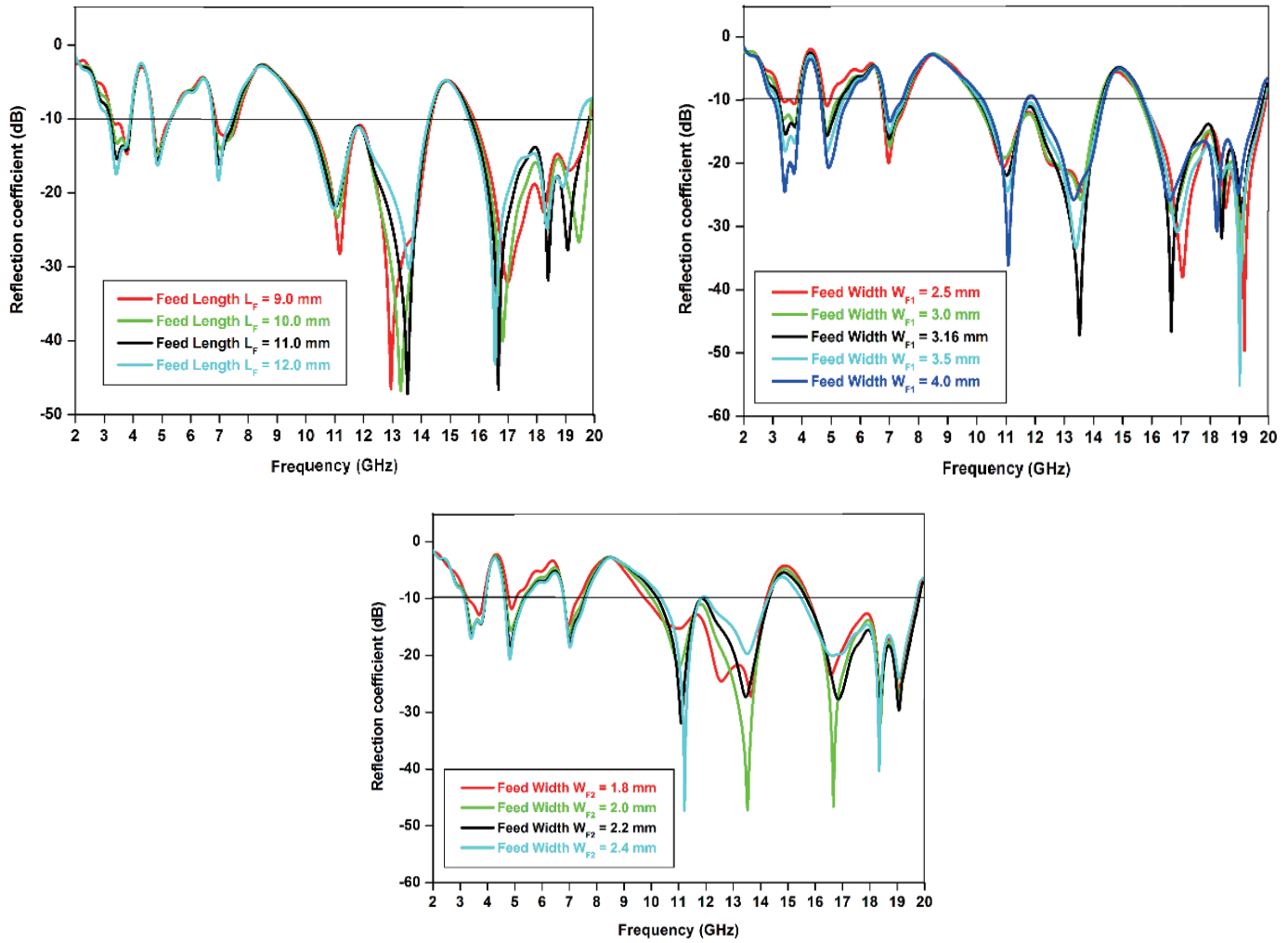


FIGURE 10. Parametric study for feedline parameters (L_F , W_{F1} and W_{F2}).

$$\text{Refractive index } (n_r) = (1/k_1 t_s) \cos^{-1} [(1/2S_{21}) \{(1 + S_{21})^2 - 2S_{21} - (S_{11})^2\}] \quad (5)$$

$$\text{Impedance } (z_i) = [\{(1 + S_{11})^2 - (S_{21})^2\} / \{(1 - S_{11})^2 - (S_{21})^2\}]^{1/2} \quad (6)$$

Wave number $k_1 = (\omega)/c$ (speed of light), Slab (substrate material) thickness = t_s .

During design evolution of proposed design, configuration C represents the modified rectangular shape SRR structure, placed at the ground plane, to achieve the penta-band resonating characteristics (from Figures 2 and 3). An additional operating band at 3.51 GHz is achieved for WiMAX application by introducing the proposed SRR cell inside the ground section. The design parameters of the proposed rectangular SRR geometry for resonant frequency f_1 are identified by the following equations:

$$P_{MRSRR-Ext} = 2(L_{1-SRR} + W_{1-SRR} - g_1) = \frac{\lambda_{gw}}{2}$$

$$= \frac{c}{2f_1 \sqrt{\epsilon_{eff}}} \quad (7)$$

$$\epsilon_{eff} = 0.5(\epsilon_r + 1) + \frac{0.5(\epsilon_r - 1)}{\sqrt{1 + \frac{12h_{subst}}{W_{feed}}}} \quad (8)$$

Here, $P_{MRSRR-Ext}$ represents the perimeter of the external modified rectangular shape split rings respectively that are function of length (L_{1-SRR}), width (W_{1-SRR}), and gap (g_1), respectively, (Figure 4(c)). For the proposed SRR to resonate at f_1 , the external perimeter $P_{MRSRR-Ext}$ should be approximately equal to half of the guided wavelength (λ_{gw}) at that respective frequency. Another parameter, the effective dielectric constant (ϵ_{eff}), is derived by using Equation (8), which is depen-

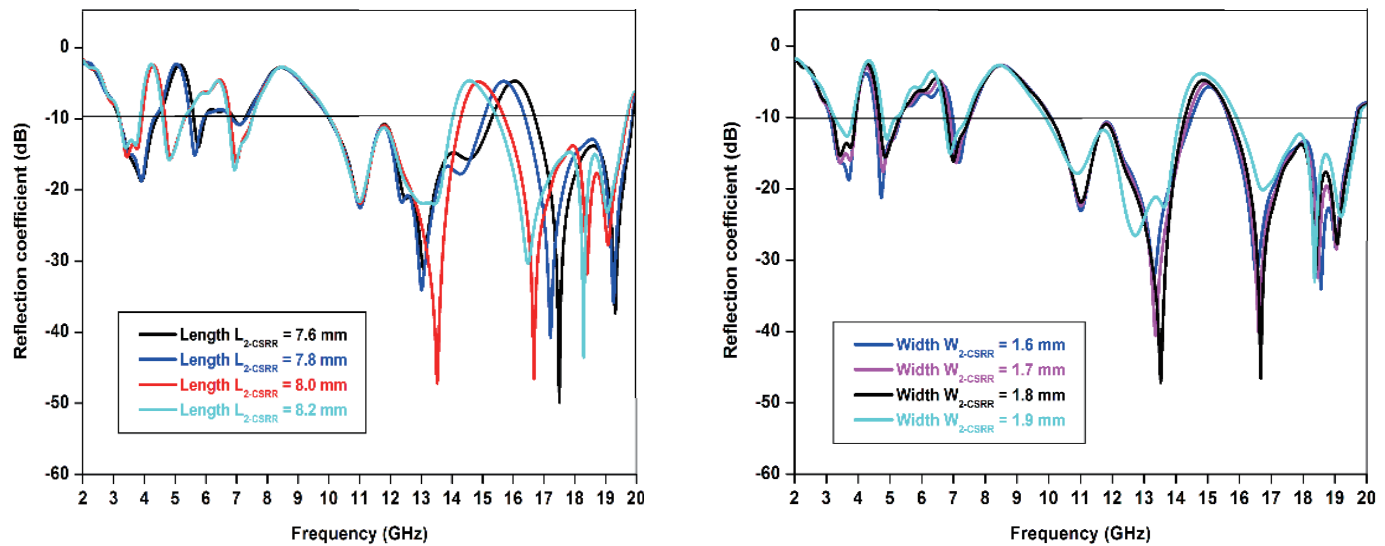


FIGURE 11. Parametric study for CSRR parameters (length L_{2-CSRR} and width W_{2-CSRR}).

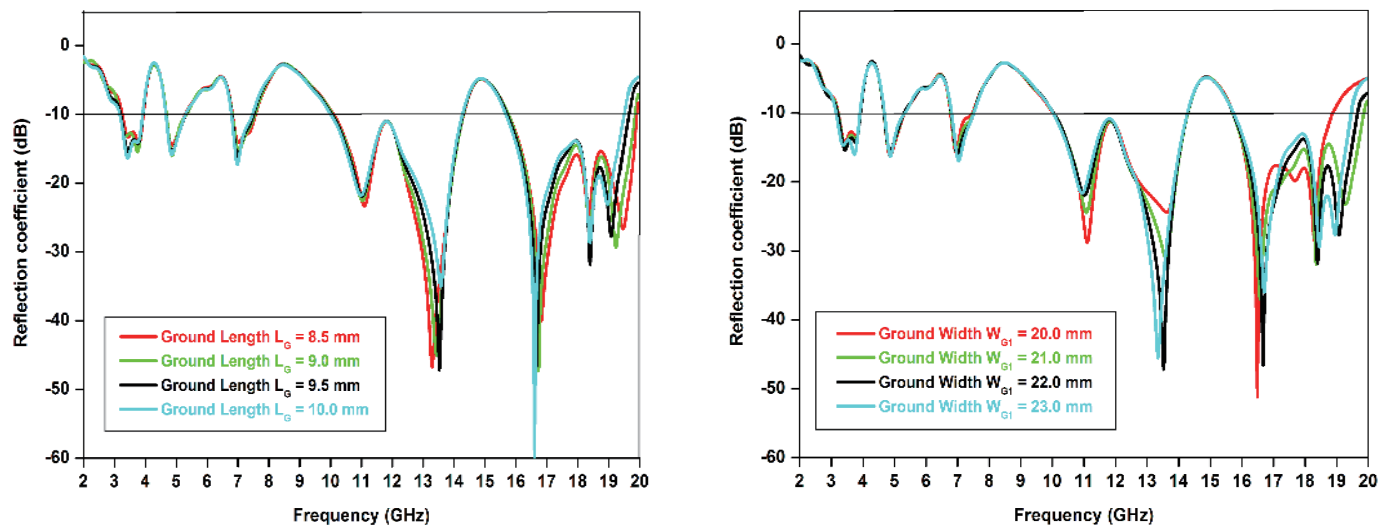


FIGURE 12. Parametric study for ground parameters (L_G and W_{G1}).

dent upon the substrate height (h_{subst}), feedline width (W_{feed}), and relative permittivity of substrate (ϵ_r), respectively [24].

The setup provides the S parameters (transmission: S_{21} and reflection coefficients: S_{11}), which are used to retrieve the effective dielectric parameters of proposed SRR [23, 24]. From Figures 15 and 16, it is observed that the SRR transmission peak (from comparison of simulated and measured S parameters) and negative permeability characteristics (from comparison of negative permeability characteristics) are achieved at 3.51 GHz. The SRR represents the single negative behavior at 3.51 GHz. The S parameter comparative plots indicate that S_{11} and S_{21} are above and below the -10 dB level respec-

tively at the resonant peak of 3.51 GHz. The comparative plot of SRR regarding negative permeability characteristics indicate the negative value of effective permeability at 3.51 GHz.

3.3. Study of CSRR Structure

The proposed CSRR structure is designed by etching two rectangular shape sections with gap at feedline. The negative dielectric property is obtained by using waveguide setup, as shown in Figure 17. The simulated setup is helpful to generate the S parameters (S_{11} and S_{12}). These parameters are used to calculate the effective permeability characteristics of meta-

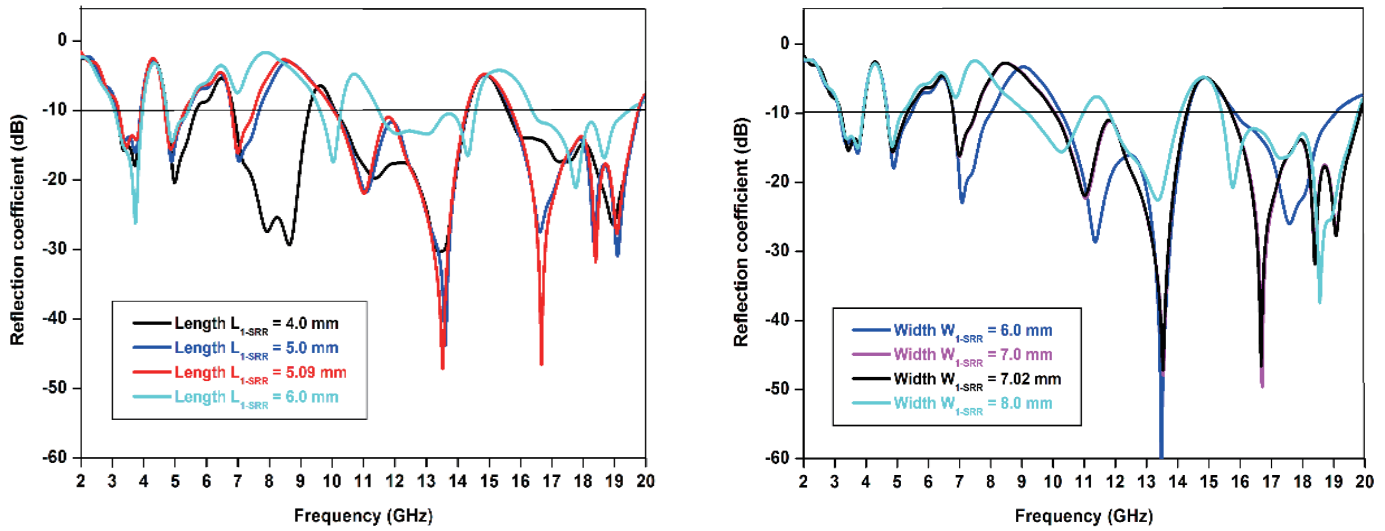


FIGURE 13. Parametric study for SRR parameters (length L_{1-SRR} and width W_{1-SRR}).

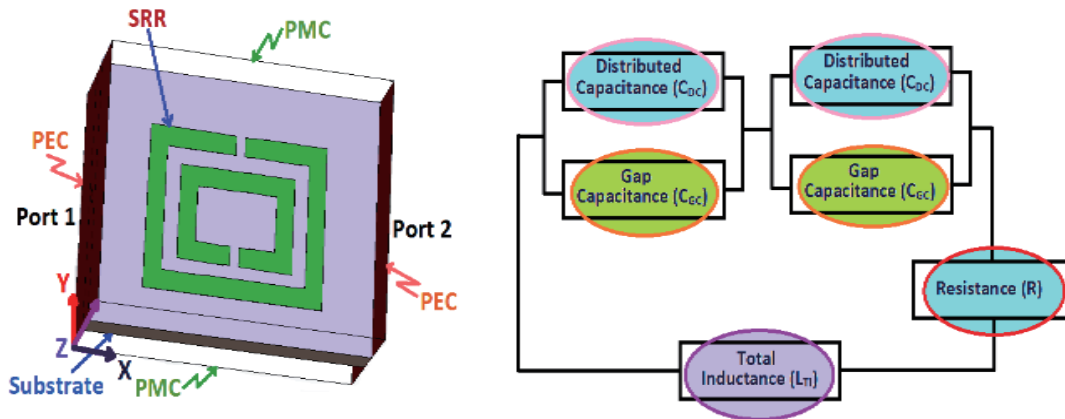


FIGURE 14. SRR structure: Simulated waveguide method and an equivalent circuit.

material cell CSRR. From Figure 18, an equivalent model of CSRR consists of inductor L_o and capacitor C_{CSRR} in parallel formation to create the resonant characteristics [25]. To retrieve the experimental S parameters, a waveguide setup is established where proposed CSRR is placed at the center position, and VNA is applied.

Inside the setup, by applying the appropriate boundary conditions as indicated in Figure 17, the operating frequency ($f_{reson-CSRR}$) is obtained as [25];

$$f_r = \frac{1}{2\pi\sqrt{L_o C_{CSRR}}} \quad (9)$$

$$C_{CSRR} = (N_p - 1)(0.5J_0) \{2L_p - (2N_p - 1)(W_p + g_2)\} \quad (10)$$

$$J_0 = \varepsilon_0 \{G(\sqrt{1 - G^2})/G(t)\} \quad (11)$$

$$t = (g_2/2)/\{(W_p) + (g_2/2)\} \quad (12)$$

$$L_o = 4\mu_0 \{ \{L_p - (N_p - 1)\} \{W_p + g_2\} [\ln(0.98/s) + 1.84s] \} \quad (13)$$

$$s = \{ \{(N_p - 1)(W_p + g_2)\} / \{1 - (N_p - 1)(W_p + g_2)\} \} \quad (14)$$

where $G(t)$ = Elliptical integration formation, N_p = No. of rings L_p = Internal ring length, W_p = Internal ring width, and g_2 = split gap.

According to the duality principle, a CSRR structure represents the dual element formation of an SRR structure. The proposed CSRR structure exhibits passband filter characteristics at 5.02 GHz. From Figure 19, the comparative plots of S parameters of CSRR cell represent the passband behavior at 5.02 GHz. S parameters are obtained by using waveguide setup [25]. The proposed CSRR cell is placed inside the waveguide setup with boundary condition of PEC (Perfect Electric Conductor) and PMC (Perfect Magnetic Conductor), as illustrated in Figure 17.

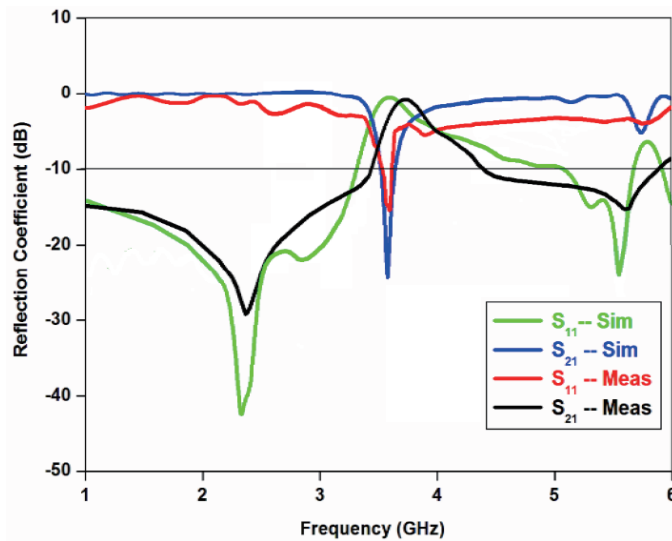


FIGURE 15. SRR Cell: Comparison of S parameters.

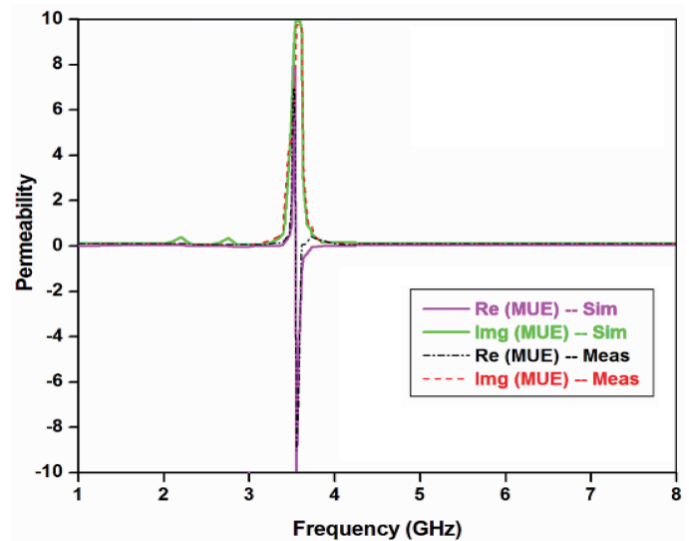


FIGURE 16. SRR Cell: Comparison of negative permeability characteristics.

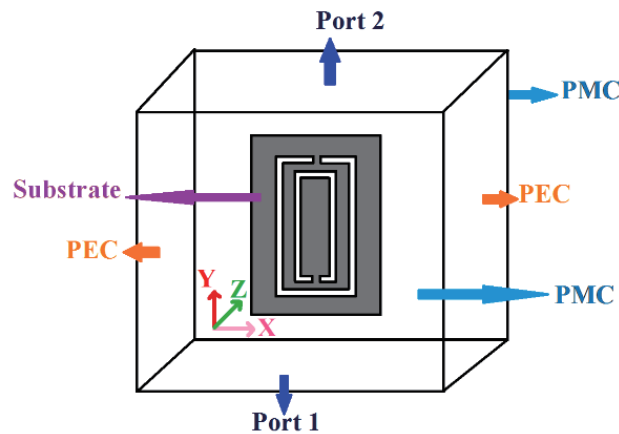


FIGURE 17. CSRR Cell: setup with boundary conditions.

The EM wave is applied at port 1, which passes through the CSRR structure, and the transmission (S_{21}) and reflection (S_{11}) coefficients are measured at port 2 by using VNA.

The proposed CSRR structure exhibits the features of magnetic resonator by which it represents the negative permeability characteristic at operating frequency 5.02 GHz. This characteristic is produced due to the orthogonal orientation of the electric field. As per the comparative analysis of S parameters from Figure 19, the transmission coefficient (S_{21} parameter) and reflection coefficient (S_{11} parameter) exist at zero level (< -1 dB) and below the reference level (-10 dB) respectively for resonant mode at 5.02 GHz. This S parameter analysis indicates the passband characteristics of proposed CSRR cell at 5.02 GHz. Another observation is related with the comparative analysis of real and imaginary sections of permittivity, as shown in Figure 20. The real section of permeability is negative for operating mode at 5.02 GHz (negative permeability features).

4. RESULT ANALYSIS

The current distributions of proposed antenna at various resonant frequencies are shown in Figure 21. It is observed that the current vectors are mostly present at SRR cell for resonant mode 3.51 GHz. For next higher operating mode 5.02 GHz, vectors are mainly allocated across the CSRR structure. The major portion of current distribution is shifted along the slotted section of radiating patch for higher resonant frequencies 6.52, 10.78, 13.57, and 16.82 GHz, as illustrated in Figure 21. It is also noticed that the proposed design achieves broadband with good impedance matching characteristics for higher resonant frequencies [26, 27].

The comparative plots of antenna peak gain and radiation efficiency of the proposed design are illustrated in Figures 22 and 23, respectively. The peak gain values and percentage radiation efficiency at various resonant frequencies and achieved wireless standards are mentioned in Table 6. From Table 6, it is noticed that the proposed design attains the maximum peak

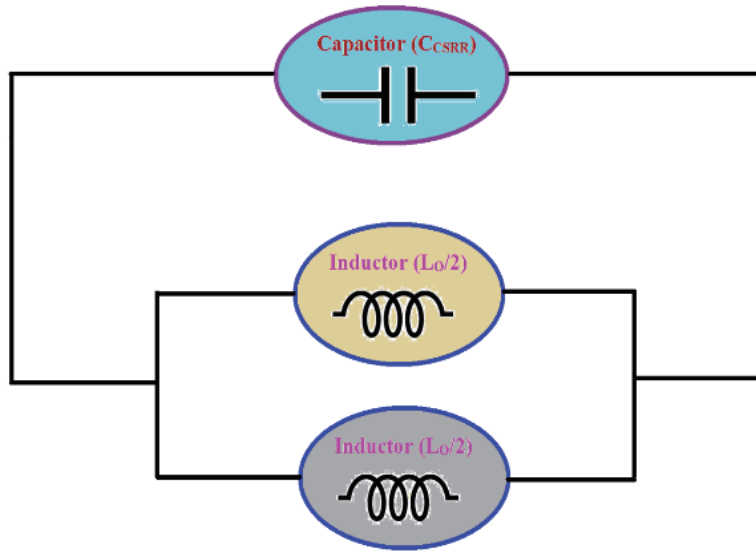


FIGURE 18. CSRR: An equivalent circuit.

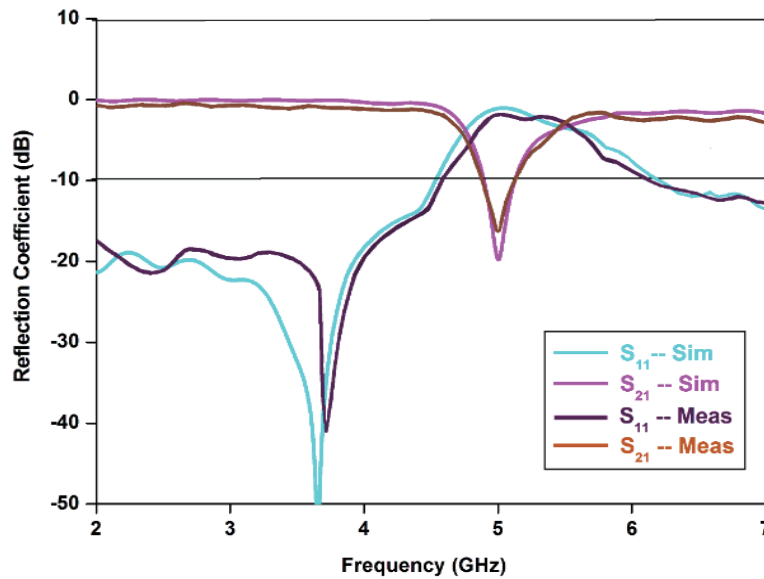


FIGURE 19. CSRR: Comparative plot of *S* parameters.

TABLE 6. Comparison of antenna peak gain and radiation efficiency (simulation and measurement mode).

Wireless Communication modes	Antenna peak gain (in dBi)		Radiation efficiency (in %)	
	Simulated	Experimental	Simulated	Experimental
WiMAX (3.51 GHz)	2.82	2.49	81.12	74.92
WLAN (5.02 GHz)	1.71	0.86	79.34	59.96
Upper C-band (6.92 GHz)	1.62	1.34	79.98	75.68
Upper X band (10.78 GHz)	2.87	2.23	76.24	73.52
Lower Ku band (13.57 GHz)	3.59	3.21	85.42	81.79
Upper Ku band (16.82 GHz)	3.62	3.32	86.52	82.06

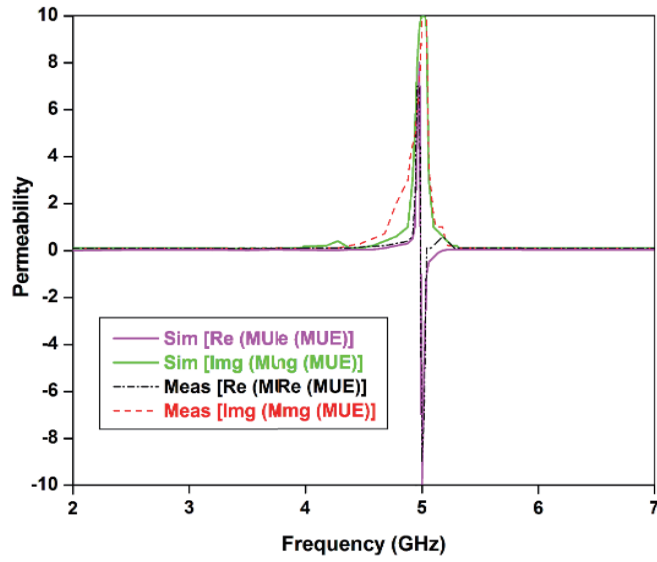


FIGURE 20. CSRR: Comparative Plot of permeability.

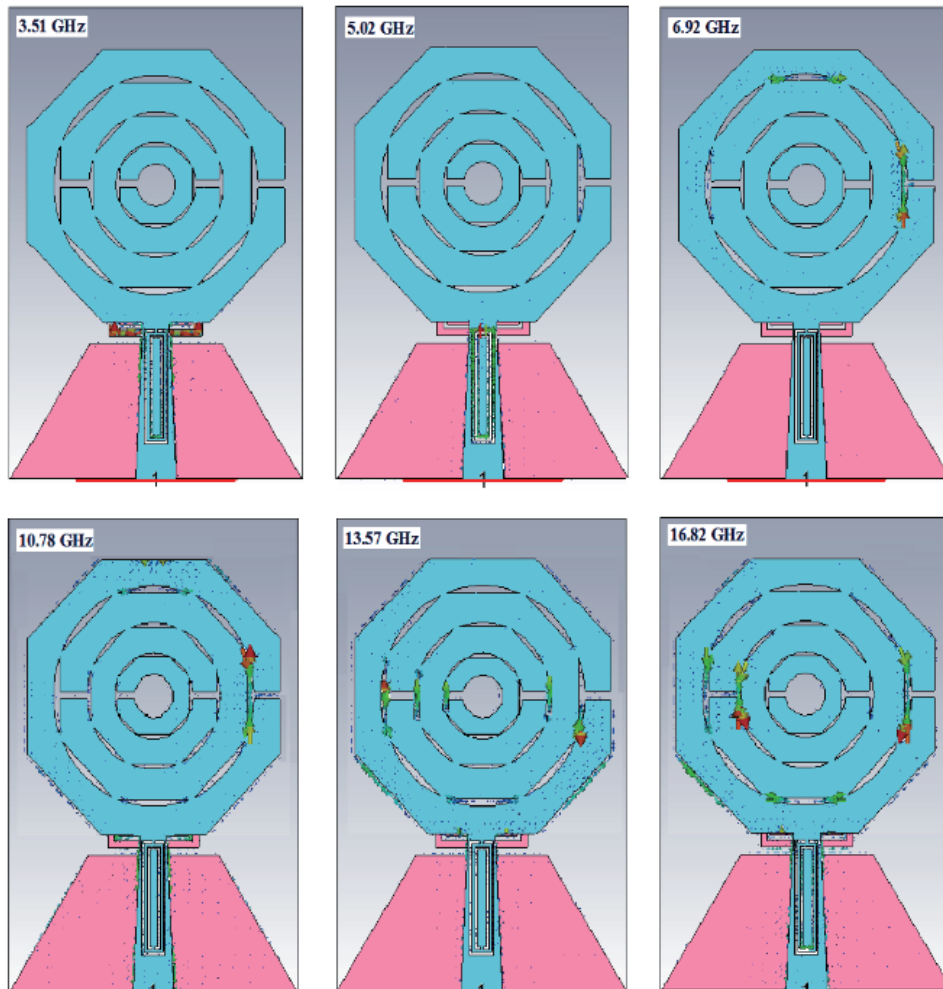


FIGURE 21. Current distribution at resonant frequencies of proposed antenna.

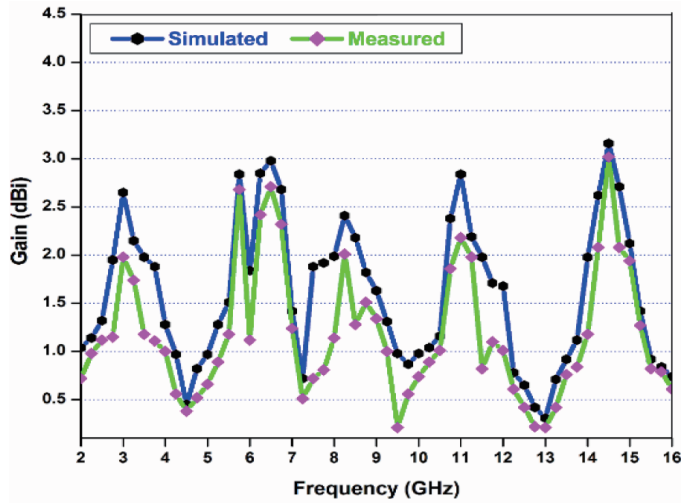


FIGURE 22. Comparative plot of antenna peak gain during simulation and measurement mode.

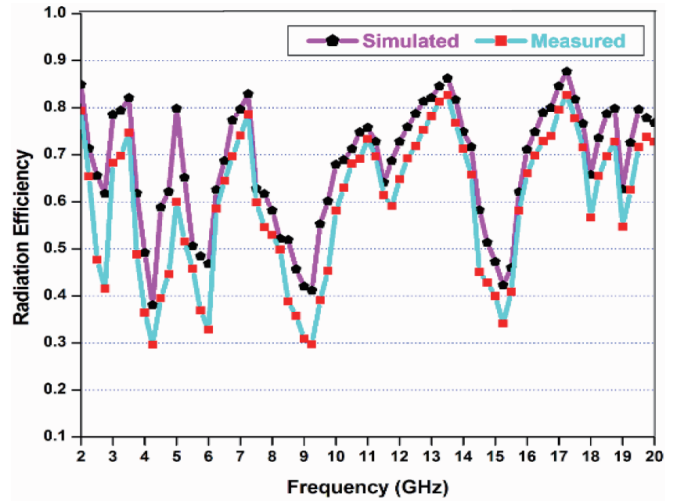


FIGURE 23. Comparative plot of antenna radiation efficiency during simulation and measurement mode.

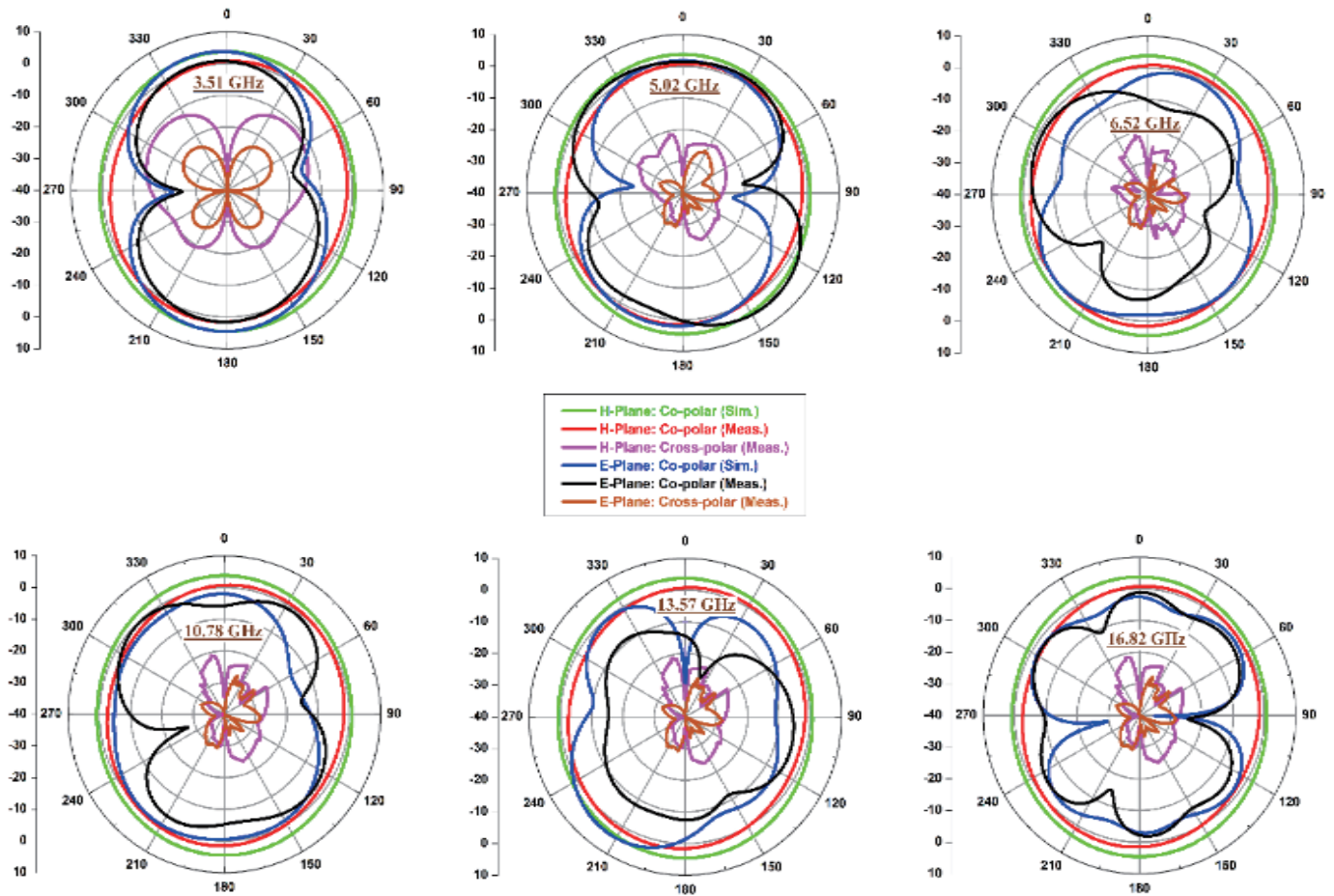


FIGURE 24. Patterns at 3.51, 5.02, 6.52, 10.78, 13.57, and 16.82 GHz.

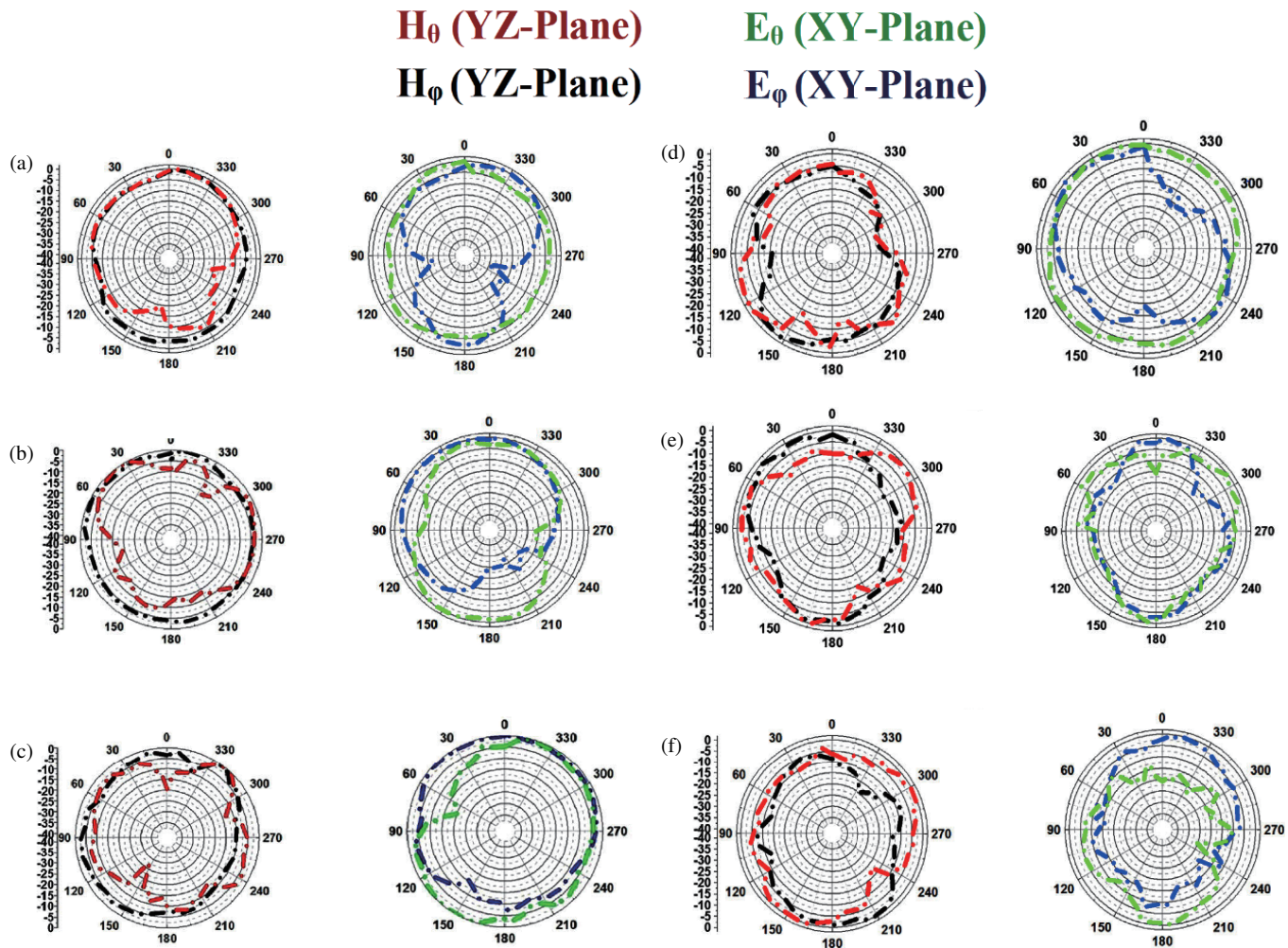


FIGURE 25. Proposed design experimental radiation E and H -plane patterns (a) 3.51 GHz, (b) 5.02 GHz, (c) 6.52 GHz, (d) 10.78 GHz, (e) 13.57 GHz, and (f) 16.82 GHz.

gain and radiation efficiency of 3.62 dBi and 86.52% at upper Ku band (16.82 GHz). It is also observed that the average efficiency of proposed design is more than 70% for all the achieved wireless standards.

The radiation patterns of proposed design regarding E and H plane (co/cross polarization mode) are plotted for various resonant modes, as illustrated in Figure 24. It is observed that the patterns are dipole like/bi-directional nature for E -plane and omnidirectional for H -plane. There is a good agreement between the simulated and experimental radiation E and H plane patterns. The antenna's radiation patterns are assessed in an anechoic chamber, with the test setup positioned at a far-field distance (i.e., $R \gg 2D^2/\lambda$, as per the Friis equation). Measurements were taken at 5° intervals from 0° to 360° in both the xy and yz planes for E and H planes, respectively, considering Co/Cross Polarization Mode. The simulated and experimental radiation characteristics of the antenna at operating frequencies of 3.51, 5.02, 6.52, 10.78, 13.57, and 16.82 GHz in both xy (E) and yz (H) planes are illustrated in Figure 24. Notably, the antenna exhibits an almost dipole-like pattern in the xy -plane and

an omnidirectional pattern in the yz -plane. Any irregularities in the pattern may be attributed to fabrication tolerances and cable losses.

The focus of the radiation characteristics is on observing the relative E/H field strength concerning the antenna design. Patterns are identified at a single frequency, single polarization, and single-plane cut. The E and H plane patterns are presented in either polar or rectilinear form, utilizing a dB strength scale. Measurement of patterns in the far field mode within the anechoic chamber is conducted using an ainfonic horn antenna (model no. LB-10180). The measured E and H -plane radiation patterns of the proposed antenna design in the $x-y$ and $y-z$ planes, under conditions of $\theta = 0^\circ$ and $\varphi = 90^\circ$, at resonant frequencies 3.51, 5.02, 6.52, 10.78, 13.57, and 16.82 GHz are depicted in Figure 25. It is observed that the antenna exhibits stable radiation characteristics with an almost omnidirectional radiation pattern in the yz -plane (H), while a bi-directional radiation pattern in the xy -plane (E) is evident at the resonating frequencies, respectively.

TABLE 7. Comparative observation of proposed design.

Reference No. and publication year	Proposed structure dimensions	SRR/CSRR Cell Implementation	Achieved bandwidth	Achieved peak Gain value	Achieved peak Efficiency value	No. of covered operating wireless bands/modes
[28] (2015)	1000 mm ³	Metamaterial CSRR structure	131.81 percentage	1.05 dBi	64.80 percentage	one
[29] (2017)	2560 mm ³	Metamaterial SRR structure	100, 109.86 percentage	6.00 dBi	70.00 percentage	two
[30] (2018)	180000 mm ³	Metamaterial SRR structure	41.97 percentage	8.00 dBi	–	one
[31] (2019)	768 mm ³	Metamaterial SRR structure	3.28, 24.95 percentage	2.28, 1.96 dBi	62.53, 93.25 percentage	two
[32] (2019)	160200 mm ³	Metamaterial SRR structure	16.13 percentage	14.00 dBi	–	one
[33] (2020)	544 mm ³	Metamaterial SRR structure	62.88 percentage	3.0 dBi	93 percentage	one
[34] (2021)	326095 mm ³	Metamaterial SRR structure	23.63 percentage	11.90 dBi	78.00 percentage	one
[35] (2021)	960 mm ³	Metamaterial CSRR structure	9.18, 34.21, 46.38 percentage	1.8, 2.5, 3.4 dBi	–	three
Proposed Antenna Structure	1161.6 mm ³	Metamaterial SRR and CSRR structure	21.54, 13.63, 10.61, 35.03, 23.74 percentage	2.51, 1.52, 1.51, 2.48, 3.58, 3.62 dBi	81.28, 79.98, 82.34, 76.84, 86.52 percentage	five

Table 7 provides the comparative analysis proposed design with previously published antenna on the basis of various characteristics of the metamaterial antennas. As per the observation from Table 7, the proposed antenna design indicates the improved antenna characteristics as compared with the available antennas in the literature.

5. CONCLUSION

The proposed metamaterial loaded penta band antenna for 5G Sub-6 GHz NR Bands and wireless applications WLAN/WiMAX/X/Ku band is designed, fabricated, and tested. The antenna shows the compactness in size with dimensions of $33 \times 22 \times 1.6 \text{ mm}^3$ and operating over the five resonating modes at 3.19–3.96 GHz, 4.65–5.33 GHz, 6.78–7.54 GHz, 10.03–14.29 GHz, and 15.74–19.98 GHz to cover the wireless standards 5G New Radio (FR1-n48/ n78/ n79/ n96), WiMAX (3.51 GHz), WLAN (5.02 GHz), Upper C-band (6.92 GHz), Upper X band (10.78 GHz), and Upper Ku band (16.82 GHz). The structure exhibits a reasonable gain and more than 70% average radiation efficiency for all the resonance bands. The negative parameter of the proposed SRR and CSRR metamaterial structure has been investigated and verified from the permeability graph. The simulated results are on par with the measured ones.

REFERENCES

- [1] Agiwal, M., A. Roy, and N. Saxena, "Next generation 5G wireless networks: A comprehensive survey," *IEEE Communications Surveys & Tutorials*, Vol. 18, No. 3, 1617–1655, 2016.
- [2] 3G PP specification series: 38 series, Online Available: <https://www.3gpp.org/Dyna Report/38-series.htm>2020.
- [3] Jin, G., C. Deng, Y. Xu, J. Yang, and S. Liao, "Differential frequency-reconfigurable antenna based on dipoles for sub-6 GHz 5G and wlan applications," *IEEE Antennas and Wireless Propagation Letters*, Vol. 19, No. 3, 472–476, 2020.
- [4] Zeng, J. and K.-M. Luk, "Single-layered broadband magneto-electric dipole antenna for new 5G application," *IEEE Antennas and Wireless Propagation Letters*, Vol. 18, No. 5, 911–915, 2019.
- [5] Sim, C. Y. D., H. Y. Liu, and C. J. Huang, "Wideband MIMO antenna array design for future mobile devices operating in the 5G NR frequency bands n77/n78/n79 and LTE band 46," *IEEE Antennas and Wireless Propagation Letters*, Vol. 19, No. 1, 74–78, 2020.
- [6] Wu, R.-Z., P. Wang, Q. Zheng, and R.-P. Li, "Compact CPW-fed triple-band antenna for diversity applications," *Electronics Letters*, Vol. 51, No. 10, 735–736, 2015.
- [7] Cao, Y. F., S. W. Cheung, and T. I. Yuk, "A multiband slot antenna for GPS/WiMAX/WLAN systems," *IEEE Transactions on Antennas and Propagation*, Vol. 63, No. 3, 952–958, 2015.
- [8] Saraswat, R. K. and M. Kumar, "A frequency band reconfigurable uwb antenna for high gain applications," *Progress In Elec-*

- tromagnetics Research B*, Vol. 64, 29–45, 2015.
- [9] Ali, T., M. M. Khaleeq, S. Pathan, and R. C. Biradar, “A multiband antenna loaded with metamaterial and slots for GPS/WLAN/WiMAX applications,” *Microwave and Optical Technology Letters*, Vol. 60, No. 1, 79–85, 2018.
- [10] Xu, H.-X., G.-M. Wang, Y.-Y. Lv, M.-Q. Qi, X. Gao, and S. Ge, “Multifrequency monopole antennas by loading metamaterial transmission lines with dual-shunt branch circuit,” *Progress In Electromagnetics Research*, Vol. 137, 703–725, 2013.
- [11] Rao, M. V., B. T. P. Madhav, T. Anilkumar, and B. P. Nadh, “Metamaterial inspired quad band circularly polarized antenna for WLAN/ISM/Bluetooth/WiMAX and satellite communication applications,” *AEU-International Journal of Electronics and Communications*, Vol. 97, 229–241, 2018.
- [12] Ali, T. and R. C. Biradar, “A compact multiband antenna using $\lambda/4$ rectangular stub loaded with metamaterial for IEEE 802.11 N and IEEE 802.16 E,” *Microwave and Optical Technology Letters*, Vol. 59, No. 5, 1000–1006, 2017.
- [13] Kukreja, J., D. K. Choudhary, and R. K. Chaudhary, “CPW fed miniaturized dual-band short-ended metamaterial antenna using modified split-ring resonator for wireless application,” *International Journal of RF and Microwave Computer-aided Engineering*, Vol. 27, No. 8, e21123, 2017.
- [14] Saraswat, R. K. and M. Kumar, “A metamaterial hepta-band antenna for wireless applications with specific absorption rate reduction,” *International Journal of RF and Microwave Computer-aided Engineering*, Vol. 29, No. 10, e21824, 2019.
- [15] Ali, T., M. Saadh, and R. C. Biradar, “A fractal quad-band antenna loaded with L-shaped slot and metamaterial for wireless applications,” *International Journal of Microwave and Wireless Technologies*, Vol. 10, No. 7, 826–834, 2018.
- [16] Rajeshkumar, V. and S. Raghavan, “SRR-based polygon ring penta-band fractal antenna for GSM/WLAN/WiMAX/ITU band applications,” *Microwave and Optical Technology Letters*, Vol. 57, No. 6, 1301–1305, 2015.
- [17] Elavarasi, C. and T. Shanmuganatham, “Multiband SRR loaded koch star fractal antenna,” *Alexandria Engineering Journal*, Vol. 57, No. 3, 1549–1555, 2018.
- [18] Ahmad, B. H. and H. Nornikman, “Fractal microstrip antenna with minkowski island split ring resonator for broadband application,” in *2013 IEEE International RF and Microwave Conference (RFM)*, 214–218, 2013.
- [19] Saraswat, R. K. and M. Kumar, “Miniaturized slotted ground UWB antenna loaded with metamaterial for WLAN and WiMAX applications,” *Progress In Electromagnetics Research B*, Vol. 65, 65–80, 2016.
- [20] Saraswat, R. K. and M. Kumar, “A vertex-fed hexa-band frequency reconfigurable antenna for wireless applications,” *International Journal of RF and Microwave Computer-aided Engineering*, Vol. 29, No. 10, 1–13, 2019.
- [21] Computer simulation technology microwave studio (CST MWS), Retrieved from <http://www.cst.co>.
- [22] Chen, H., J. Zhang, Y. Bai, Y. Luo, L. Ran, Q. Jiang, and J. A. Kong, “Experimental retrieval of the effective parameters of metamaterials based on a waveguide method,” *Optics Express*, Vol. 14, No. 26, 12944–12949, 2006.
- [23] Saha, C. and J. Y. Siddiqui, “Versatile cad formulation for estimation of the resonant frequency and magnetic polarizability of circular split ring resonators,” *International Journal of RF and Microwave Computer-aided Engineering*, Vol. 21, No. 4, 432–438, 2011.
- [24] Smith, D. R., D. C. Vier, T. Koschny, and C. M. Soukoulis, “Determination of negative permittivity and permeability of metamaterials from reflection and transmission coefficients,” *Phys. Rev. B*, Vol. 65, 5104–5109, 2002.
- [25] Bilotti, F., A. Toscano, L. Vegni, K. Aydin, K. B. Alici, and E. Ozbay, “Equivalent-circuit models for the design of metamaterials based on artificial magnetic inclusions,” *IEEE Transactions on Microwave Theory and Techniques*, Vol. 55, No. 12, 2865–2873, 2007.
- [26] Saraswat, R. K. and M. Kumar, “Implementation of hybrid fractal metamaterial inspired frequency band reconfigurable multiband antenna for wireless applications,” *International Journal of RF and Microwave Computer-aided Engineering*, Vol. 30, No. 9, 1–19, 2020.
- [27] Saraswat, R. K. and M. Kumar, “A quad band metamaterial miniaturized antenna for wireless applications with gain enhancement,” *Wireless Personal Communications*, Vol. 114, No. 4, 3595–3612, 2020.
- [28] Islam, S. S., T. Alam, M. R. I. Faruque, and M. T. Islam, “Design and analysis of a complementary split ring resonator (CSRR) metamaterial based antenna for wideband application,” *Science and Engineering of Composite Materials*, Vol. 24, No. 4, 573–580, 2017.
- [29] Heydari, S., K. Pedram, Z. Ahmed, and F. B. Zarrabi, “Dual band monopole antenna based on metamaterial structure with narrowband and UWB resonances with reconfigurable quality,” *AEU-International Journal of Electronics and Communications*, Vol. 81, 92–98, 2017.
- [30] Sinha, M., V. Killamsetty, and B. Mukherjee, “Near field analysis of rdra loaded with split ring resonators superstrate,” *Microwave and Optical Technology Letters*, Vol. 60, No. 2, 472–478, 2018.
- [31] Garg, P. and P. Jain, “Design and analysis of a metamaterial inspired dual band antenna for WLAN application,” *International Journal of Microwave and Wireless Technologies*, Vol. 11, No. 4, 351–358, 2019.
- [32] Pandey, A. K., M. Chauhan, V. K. Killamsetty, and B. Mukherjee, “High-gain compact rectangular dielectric resonator antenna using metamaterial as superstrate,” *International Journal of RF and Microwave Computer-aided Engineering*, Vol. 29, No. 12, 1–10, 2019.
- [33] Ameen, M., A. Mishra, and R. K. Chaudhary, “Asymmetric CPW-fed electrically small metamaterial-inspired wideband antenna for 3.3/3.5/5.5 GHz WiMAX and 5.2/5.8 GHz WLAN applications,” *AEU-International Journal of Electronics and Communications*, Vol. 119, 153177, 2020.
- [34] Chauhan, M., A. Rajput, and B. Mukherjee, “Wideband circularly polarized low profile dielectric resonator antenna with meta superstrate for high gain,” *AEU-International Journal of Electronics and Communications*, Vol. 128, 153524, 2021.
- [35] Sharma, N., A. Kumar, A. De, and R. K. Jain, “Design of compact hexagonal shaped multiband antenna for wearable and tumor detection applications,” *Progress In Electromagnetics Research M*, Vol. 105, No. 2021, 205–217, 2021.
- [36] Mu, W., Z. Wang, M. Yang, W. Nie, and P. Wang, “A six-port slot antenna system with wideband and high-isolation for 5G NR bands,” *Progress In Electromagnetics Research M*, Vol. 107, 105–118, 2022.
- [37] Jiang, J.-Y. and H.-L. Su, “A wideband eight-element MIMO antenna array in 5G NR n77/78/79 and WLAN-5 GHz bands for 5G smartphone applications,” *International Journal of Antennas and Propagation*, Vol. 2022, 2022.
- [38] Murugan, C. and T. Kavitha, “A compact four-element modified annular ring antenna for 5G applications,” *Progress In Electromagnetics Research C*, Vol. 137, 2023.

- [39] Sharma, Y., H. H. Zhang, and H. Xin, "Machine learning techniques for optimizing design of double T-shaped monopole antenna," *IEEE Transactions on Antennas and Propagation*, Vol. 68, No. 7, 5658–5663, 2020.
- [40] El Misilmani, H. M., T. Naous, and S. K. A. Khatib, "A review on the design and optimization of antennas using machine learning algorithms and techniques," *International Journal of RF and Microwave Computer-aided Engineering*, Vol. 30, No. 10, e22356, 2020.
- [41] Sallam, T., A. B. Abdel-Rahman, M. Alghoniemy, Z. Kawasaki, and T. Ushio, "A neural-network-based beamformer for phased array weather radar," *IEEE Transactions on Geoscience and Remote Sensing*, Vol. 54, No. 9, 5095–5104, 2016.
- [42] Wang, J. R., W. J. Liu, and M. S. Tong, "An artificial neural network based design of triple-band microstrip patch antenna for WLAN applications," in *2020 IEEE MTT-S International Conference on Numerical Electromagnetic and Multiphysics Modeling and Optimization (NEMO)*, 1–4, 2020.
- [43] Training and Test Sets: Splitting Data. Machine Learning Crash Course, [Online], Available: <https://developers.google.com/machine-learning/crash-course/training-and-test-sets/splitting-data>.